International Journal of Computational and Experimental Science and ENgineering (IJCESEN)

Vol. 11-No.4 (2025) pp. 10241-10253
http://www.ijcesen.com

ISSN: 2149-9144

Research Article

Fast and Large-Scale Brain Hemorrhage Detection Using RKNODE U-Net and Enhanced Blending RKNODE M-Net with Cloud Integration

D. Jeni Jeba Seeli[1]*, K. K. Thanammal[2]

[1]Research Scholar, Department of Computer Science, S.T Hindu College,Nagercoil, Pin: 629 002, Affiliated to Manonmaniam Sundaranar University, Tamil Nadu, India.
* **Corresponding Author Email:** jeniseeli@gmail.com - **ORCID:** 0000-0002-3839-8072

[2] Assistant Professor, Department of Computer Science, S.T Hindu College,Nagercoil Pin: 629 002, Affiliated to Manonmaniam Sundaranar University, Tamil Nadu, India.
Email: thanamma2l@gmail.com- **ORCID:** 0009-0005-2224-1539

Article Info:

DOI: 10.22399/ijcesen.4820
Received : 20 October 2025
Revised : 06 December 2025
Accepted : 13 December 2025

Keywords

Cloud Environment,
Runge Kutta Method,
U-Net Segmentation,
Particle Swarm Optimization.

Abstract:

Brain hemorrhage, a critical kind of stroke resulting from ruptured blood vessels, necessitates prompt identification and intervention to mitigate death rates. This research presents a rapid and scalable method for bleeding detection utilizing the RSNA brain hemorrhaging dataset, integrating sophisticated deep learning techniques with a cloud-based platform for effective training, storage, and global accessibility. A hybrid approach employing ResNet50, DenseNet121, and VGG16 is implemented for feature extraction, while a novel quantum-behaved particle swarm optimizing technique utilizing differential equations is introduced for feature selection, enabling efficient exploration, reduced density, and stable convergence. The chosen characteristics are integrated and classified utilizing a fourth-order Runge-Kutta Neural ODE meta-network, thereby augmenting classification resilience via adaptive depth modelling. A U-Net architecture augmented with a Runge–Kutta ODE block in the bottleneck is employed for RSNA CT image segmentation to accurately localize hemorrhagic regions, enabling segmentation-guided feature learning that enhances downstream classification performance despite the absence of pixel-level annotations in the RSNA dataset. The segmented regions further allow estimation of hemorrhage size and localization. The results of experiments on benchmark datasets indicate enhanced classification and segmentation accuracy, less redundancy, increased prediction speed and improved efficiency compared to traditional methods, underscoring the framework's possibility of real-time large-scale clinical application.

1. Introduction

Brain hemorrhage classification involves identifying and categorizing hemorrhage types from medical images. It occurs when blood accumulates in the brain due to ruptured vessels. Accurate and timely detection is crucial for effective treatment and better outcomes. Common types include intracerebral, subarachnoid, subdural, epidural, and intraventricular hemorrhages, each requiring distinct interventions [1]. In the medical field, classification is vital for accurate diagnosis and guiding appropriate treatment. Different types of hemorrhage require specific interventions, and early detection can improve patient outcomes. Automated classification using machine learning and deep neural networks supports radiologists by providing faster and more reliable analysis of CT and MRI scans [2]. The principal of neuro-intensivists is to diminish morbidity and mortality associated with cerebral hemorrhages. Research must advance to accommodate the increasing intricacy of diagnostic pathways to assist clinical practice. Deep learning has increased medical image processing precision, efficiency, dependability and scalability for improving diagnostic and treatment procedures [3].Cloud-based classification leverages cloud computing for scalable, flexible, and portable machine learning, especially beneficial for medical image tasks like brain hemorrhage categorization. It efficiently stores, processes, and analyzes large datasets, overcoming limitations of local systems [4]. Cloud-based systems provide high-performance computing resources (CPUs, GPUs, specialized hardware) crucial for processing large medical image datasets (CT/MRI scans) in deep learning. This facilitates faster model training, testing, and refinement, vital for timely diagnoses in clinical settings [5]. Cloud infrastructure facilitates seamless collaboration and data/model sharing among medical professionals and researchers, improving detection and classification of conditions like brain hemorrhages. This enables healthcare providers to securely and cost-effectively deploy predictive models, extending automated classification tools to remote or resource-limited clinical settings [6]. Cloud image storage centrally manages and stores digital images on remote cloud servers, offering scalability, accessibility, and security. This method allows users to store images virtually, providing easy, internet-based access from any location [7].In deep learning, a blending ensemble combines predictions from multiple models, each extracting distinct data patterns, to improve overall performance, reliability, and accuracy. This methodology alleviates the limitations of individual models, improves generalization, diminishes overfitting, and enhances the model's capacity to manage intricate datasets [8]. Blending ensembles teach and meta-model in deep learning. Different models for deep learning are trained separately on the same dataset. In the meta-modelling phase, a basic model is trained to incorporate these base models' prediction as input characteristics to optimize ensemble accuracy [9].Neural networks and numerical methods are crucial in modern deep learning and computational mathematics, especially for dynamic systems, differential equations, and optimization. Neural networks excel at pattern recognition and tasks like classification, while numerical methods like Runge-Kutta and finite difference methods solve differential equations and optimize algorithms. Their convergence is prominent in Neural ODEs, where a network's hidden states evolve continuously via a learned differential equation. Here, numerical methods like Runge-Kutta are vital for solving these ODEs, enabling continuous-time dynamics modeling for tasks like time-series analysis and irregularly spaced data, offering flexibility and memory efficiency [10]. Numerical methods, particularly optimization algorithms like gradient descent, are essential for training neural networks by numerically differentiating and minimizing loss functions. Recent advances in neural network architectures, notably Neural ODEs, have significantly improved identification and classification capabilities, offering more accurate and interpretable models to aid in diagnosis [11]. The current CNN architecture relies on U-Nets—encoder-decoder networks with skip connections—but lacks theoretical guarantees and struggles with discrete layer limitations. Continuous U-Net, a dynamic neural network using second-order ordinary differential equations (ODEs), addresses these issues by offering theoretical support, faster convergence, improved robustness, and lower noise sensitivity. It also enables qualitative metrics tailored to specific segmentation tasks [12].

2. Literature Review

The article [13] developed a self-attention based neural network to detect for the subtype classification of cerebral hemorrhages in CT scans. This methodology incorporates an attention process leveraging ResNet for extracting features, PCA for optimal feature selection, and an XGBoost model for classification, assessed on the RNSA dataset. Three different kinds of deep neural networks GoogLeNet, ResNet and Inception are used in [14] for diagnosing the status of the brain haemorrhage classification. This approach was tested on 100 images and According to the experimental findings, these neural can diagnose brain haemorrhage disease. Authors [15] developed HResNet-based architectures for haemorrhage detection and grading using 22,811 CT scans from the CQ500 dataset. Their comparison of HResNet, HResNet-SE, and HRaNet showed that HRaNet achieved the best performance with remarkable metrics. A deep neural approach for haemorrhagic detection in brain images. Their method involves a two-step lightweight convolutional model, trained on data from multiple sources. First, they utilize the VGG-16 architecture to process the input CT scans. Subsequently, they feed the resulting data frames into a Random Forest algorithm for stroke segmentation, classifying the results into three levels [16]. The paper [17] investigated a hybrid machine learning strategy for more reliable intracranial haemorrhage diagnosis. Their research employed VGG16 and VGG19 for feature extraction from brain CT images, and then utilized these features to train Random Forest and Multilayer Perceptron models. Their study was conducted on a dataset comprising 2,501 CT brain images across five haemorrhage types. The work [18] presents an ensemble method that combines outputs from various layers or branches of a CNN. Their specific implementation involves dividing the VGG16 network into five distinct branches to capture fine-grained spatial features aligned with the deep learning network's hierarchy. However, the authors warn that combining all of these branch models into one ensemble may result in a lack of variation among the individual classification algorithms, which could impair the ensemble's capacity for generalization effectively and produce subpar results. In paper [19], the authors addressed the Internet of Things based detection of COVID using medical CT images. Initially, they collected and categorized CT images into four classes, further grouping them into disease and non-disease categories with expert physician input. Notably, they employed an image blending technique to merge features from images. Authors [20] introduced a multi-subnetwork methodology for breast cancer diagnosis with the MIAS dataset, attaining a remarkable accuracy of 99.5%; yet, their model lacked segmentation, hence constraining spatial comprehension of lesion regions. Similarly, various deep convolutional architectures including VGG16 & 19, ResNet50, InceptionV3, Xception, MobileNet and InceptionResNetV2 on the BreakHis dataset for breast cancer classification, reporting a 93.8% accuracy in [21]. The authors [22] addressed texture defect detection using a combination of MPF-DNN, ResNet101, and SVM on the TILDA dataset, achieving 95.82% accuracy; however, they did not detail their feature selection process, limiting reproducibility. Khan et al. [23] focused on heart disease classification using a large dataset and introduced two models EnsCVDD-Net and BlCVDD-Net which contains large data set and achieved 88% and 91% accuracy, respectively. Despite the large data size, the models showed relatively modest accuracy. Finally, Deo et al. [24] developed a ResNet50 and DenseNet201-based framework for oral cancer detection on the NDB-UFES dataset, achieving 92% accuracy, though the dataset's small and imbalanced nature poses limitations for generalization. Because ODE solvers are computationally demanding, the continuous nmODE model is less efficient than traditional discrete models, despite achieving robustness and higher precision with a clean training dataset. The nmODE-KD method improves efficiency and durability by distilling information from the continuous nmODE into a separate layer, minimizing the KL divergence so the latter closely mimics the former [25]. An ensemble mechanism was designed to enhance U-Net's performance, while the Convolutional segmentation technique was introduced to tackle semantic segmentation challenges in U-Net. The study utilized head CT scans from 40 patients exhibiting abnormal cerebral hemorrhage [26]. A novel model was trained using standard CT images by combining the U-Net architecture with a Dice loss method. Data preprocessing and augmentation were applied to prevent the overfitting problem. The model's segmentation performance was objectively assessed using various metrics to evaluate the precision of intracerebral hemorrhage (ICH) detection [27]. This study [28] proposed a unique CNN-based model for segmenting hematoma regions in CT scans of ICH. To address severe pixel imbalance, a multi-objective optimization function was introduced, enhancing training efficiency. The model demonstrated superior performance compared to previous methods, achieving effective and accurate segmentation for ICH detection. Table 1 provides a summary of related studies highlighting several prominent disease diagnosis systems.

Our proposed work aims to address the limitations found in the reviewed studies.

- The proposed method employs advanced preprocessing techniques, including image format conversion, intensity normalization, data augmentation, and skull stripping, to enhance input image quality and improve the effectiveness of the segmentation process.
- To minimize computational complexity, fourth-order Runge-Kutta Neural Ordinary Differential Equations with U-Net (RKNODE U-Net) and fourth-order Runge-Kutta Neural Ordinary Differential Equations with meta neural networks (RKNODE M-Net) are designed as efficient algorithms for segmentation and multi-class classification, respectively.
- For the purpose of further improving the classification accuracy, Quantum Behaved Particle Swarm Optimization with Differential Equations (QPSODE) feature selection is utilized.
- A cloud-based approach is employed to ensure efficient handling of large datasets, accelerate model training times, and facilitate seamless deployment for real-time medical imaging analysis.

3. Proposed Work

This section provides a detailed procedure for detecting brain hemorrhages based on segmentation and classification, utilizing the RKNODE U-Net and RKNODE M-Net architectures and a cloud management system. The overall structure of the proposed method illustrated in Figure 1.

The figure 1 illustrates a unified segmentation–classification framework for brain hemorrhage detection using RSNA and PhysioNet datasets. Initially, RSNA CT images undergo preprocessing and augmentation. This dataset is then split into training, validation, and testing sets in a 60:10:30 ratio to ensure robust model evaluation. In parallel, an ICH segmentation dataset is used to train an RKNODE U-Net, which produces segmented hemorrhage outputs. This trained segmentation model is then applied to RSNA images to localize hemorrhagic regions. Post-processing extracts clinically meaningful attributes such as region location and volume. The segmentation-guided outputs are fed into multiple deep CNNs (ResNet50, VGG16, and DenseNet121) for feature extraction. These features are combined and optimized using QPSODE-based feature selection before classification through an RKNODE M-Net. Finally, the model is evaluated, deployed in a cloud EC2 environment, and assessed through performance metrics and prediction visualizations, demonstrating an end-to-end cloud-enabled hemorrhage detection system.

3.1 Materials

The RSNA hemorrhage dataset contains only slice-level classification annotations and does not provide pixel-wise segmentation masks. It includes DICOM CT slices and a CSV file. The labels are for five types of hemorrhage: Epidural Hemorrhage (EH), Intraparenchymal Hemorrhage (IH), Intraventricular Hemorrhage (IVH), Subdural Hemorrhage (SH), and Subarachnoid Hemorrhage (SAH). To enable supervised training of the hemorrhage segmentation model, the PhysioNet Head CT hemorrhage dataset featuring expert annotated pixel-level segmentation masks was employed for training the segmentation network.
The CT ICH segmentation dataset is a processed version of the PhysioNet hemorrhage dataset. It consists of 2,814 pairs of CT images and corresponding segmentation masks. The data in the image and label folders are provided as 512 × 512 grayscale PNG files.

3.2 Segmentation

Since the RSNA Intracranial Hemorrhage dataset provides only slice-level classification labels and does not include pixel-wise segmentation annotations, it cannot be directly used to train supervised segmentation models. To address this limitation, the PhysioNet Head CT Hemorrhage dataset is selected for hemorrhage segmentation, as it contains expert-annotated ground-truth masks that accurately delineate hemorrhagic regions. This dataset enables effective training of segmentation architectures such as U-Net and its advanced variants, including attention-based and Runge–Kutta Neural ODE enhanced U-Net models. Because both PhysioNet and RSNA datasets consist of non-contrast head CT images with similar anatomical structures and intensity distributions, models trained on PhysioNet generalize well to RSNA images. The trained segmentation model is subsequently applied to RSNA CT slices to localize hemorrhage regions, generate region-of-interest masks, and produce masked or cropped images. These segmentation-guided outputs are then utilized for downstream hemorrhage classification and ensemble learning. This cross-dataset training strategy is a well-established and widely accepted approach in medical imaging research when large-scale classification datasets lack pixel-level annotations.

3.2.1 Segmentation using RKNODE U-Net

The RK Neural ODE block models the continuous evolution of feature maps within the U-Net bottleneck by replacing discrete convolutions with a differential equation-based update. The ODEFunc class defines a learnable function $f(x)$ using two convolutional layers with batch normalization and ReLU, capturing how feature representations change over infinitesimal steps while preserving spatial resolution and channel consistency. The RKNODE Block employs the classical fourth-order Runge–Kutta solver, computing four intermediate slopes (k1, k2, k3 and k4) along the feature trajectory and combining them to produce a stable and accurate bottleneck update. This approach enables the network to model complex, smooth transformations more effectively than simpler solvers such as Heun. To numerically approximate the solution of the above differential equation, the classical fourth-order Runge–Kutta method is employed. Given an initial feature map $a_n$and a step size h, the intermediate slopes are computed as defined in Equations (1) – (4).

$$k_1 \quad = f(a_n) \tag{1}$$

$$k_2 \quad = f\left(a_n + \frac{h}{2} k_1\right) \tag{2}$$

$$k_3 \quad = f\left(a_n + \frac{h}{2} k_2\right) \tag{3}$$

$$k_4 \quad = f(a_n + h k_3) \tag{4}$$

The output of the RK4 Neural ODE block is obtained by combining the intermediate slopes, as shown in Equation (5).

$$a_{n+1} = a_n + \frac{h}{6}(k_1 + 2k_2 + 2k_3 + k_4)$$ (5This

equation produces a stable and accurate approximation of the continuous feature evolution within the bottleneck layer.

3.2.2 Integration into U-Net bottleneck

Let $a_b$denote the bottleneck feature map produced by the convolutional encoder. The final refined bottleneck representation after RKNODE processing is given in Equation (6).

$$\hat{a}_b = \mathrm{RK4}(a_b) \quad (6)$$

where RK(·)represents the numerical integration defined above. In the U-Net architecture, the RKNODE block is placed after the bottleneck convolution, which expands feature channels to increase representational capacity. The RK block refines these high-level features through continuous time dynamics, enabling the network to capture subtle hemorrhage boundaries and irregular shapes. Fully differentiable and implemented with standard PyTorch operations, it allows end-to-end training via backpropagation. By producing smoother and more stable feature transformations, the RK based bottleneck enhances segmentation accuracy, preserves fine-grained spatial details, and improves Dice and IoU scores, particularly for small or diffuse hemorrhagic regions in CT images

The output of the proposed RKNODE-U-Net segmentation model is a pixel-wise probability map that indicates the likelihood of hemorrhage presence at each spatial location of the CT image. For an input CT slice $I_m \in \mathbb{R}^{h\times w}$, the network produces an output feature map $\widehat{Y_{out}} \in [0,1]^{h\times w}$after the final convolution and sigmoid activation. Each pixel value $\widehat{Y_{out}}_{i,j}$represents the predicted probability that the corresponding pixel belongs to a hemorrhagic region. The segmentation output is mathematically expressed in Equation (7).

$$\widehat{Y_{out}} = \sigma(W * F_{\mathrm{dec}}(I_m) + b) \quad (7)$$

where $F_{\mathrm{dec}}(I)$denotes the decoder output features after RKNODE enhanced bottleneck processing, $W$and $b$are the learnable parameters of the final 1×1 convolution, $*$represents convolution, and $\sigma(\cdot)$is the sigmoid activation function. The final binary segmentation mask is obtained by applying a thresholding operation to the probability map, as defined in Equation (8).

$$Y_{\mathrm{segout}}(i,j) = \begin{cases} 1, & \text{if } \widehat{Y_{out}}_{i,j} \geq \tau \\ 0, & \text{otherwise} \end{cases} \quad (8)$$

where τ is typically set to 0.5. The resulting binary mask Y_{segout} clearly delineates hemorrhage regions from the background. The segmentation output enables accurate hemorrhage localization, supports ROI generation for classification models, and is evaluated using DSC, IoU, sensitivity, and precision demonstrating the effectiveness of the RKNODE based approach in capturing fine grained hemorrhage patterns.

3.2.3 Connecting the Segmentation Output to the RSNA Dataset for RSNA Segmentation

Since the RSNA Intracranial Hemorrhage dataset provides only slice-level classification labels without pixel-wise annotations, the trained RK4-ODE-U-Net is used as a hemorrhage localization module. After being trained on the PhysioNet dataset, the model is directly applied to RSNA CT slices using identical preprocessing steps, including resizing, intensity normalization, and windowing to maintain domain consistency. For each RSNA CT slice I_{rsna}, the trained segmentation network produces a pixel-wise probability map $\hat{y}_{rsna}$, representing the likelihood of hemorrhage at each spatial location. By applying a predefined threshold, this probability map is converted into a binary segmentation mask Y_{segout}, which delineates the suspected hemorrhagic regions.

The generated segmentation masks are used to form segmentation-guided representations of RSNA CT images. The binary mask is multiplied element-wise with the original slice to emphasize hemorrhagic regions while suppressing background tissue connected hemorrhage regions are cropped to obtain region-of-interest (ROI) patches. These masked or cropped images are then provided as inputs to RSNA classification models such as ResNet, DenseNet, or ensemble networks. This integration bridges segmentation and classification by directing the classifier's attention to clinically relevant regions, reducing noise reducing prediction time and improving prediction accuracy. This cross-dataset technique is well-accepted since the model for segmentation is trained on PhysioNet with pixel-level labels and used to the RSNA dataset to create a coordinated hemorrhage detection framework.

3.2.4 Post Processing

After segmenting the images, we identified the bleeding regions and determined their sizes. The volume of each bleeding area was obtained by multiplying the number of voxels within it by the size of each voxel, yielding the result in cubic millimeters. In accordance with scanning protocols, this approach ensures accurate volume measurements.

3.3 Classification

The integration of segmentation output into the RSNA classification pipeline significantly enhances detection performance by guiding the classifier toward hemorrhage-relevant regions. Without segmentation, classification models process entire CT slices, which include substantial irrelevant anatomical information such as skull structures and normal brain tissue. This increases noise and prediction time and reduces discriminative learning. By contrast, segmentation-guided masked images and ROI crops focus the classification network exclusively on hemorrhagic regions, leading to improved feature representation and reduced false positives. As a result, the segmentation-assisted framework achieves higher accuracy, sensitivity, and area under the curve (AUC) compared to classification using raw CT images alone.

RSNA classification was compared to raw CT image classification utilizing segmentation-guided inputs. All assessment criteria show that masked CT images and ROI-based sources outperform genuine CT slices. Segmentation-guided classification lowers background noise and focuses on clinically significant bleeding patches, improving sensitivity and reducing false positives. Ensemble learning and ODE-based meta-classification boost resilience and generalization. This shows that segmentation knowledge, even pseudo-labels, improves classification performance on datasets without pixel-level annotations.

3.3.1 Feature Extraction using Base Models

In brain hemorrhage detection, pretrained CNNs such as ResNet50, VGG16, and DenseNet121 are used for feature extraction. ResNet50 efficiently trains deep networks using residual connections, DenseNet121 promotes feature reuse with fewer parameters, and VGG16, though computationally heavier, remains effective in certain cases. Overall, ResNet50 and DenseNet121 provide a better balance between accuracy and efficiency. These ImageNet-pretrained models are adapted by removing their classification layers to extract deep feature vectors from preprocessed brain hemorrhage PNG images. The extracted features from each network are stored independently and can be fused or concatenated. Finally, the feature vectors along with image labels are organized into a structured dataset (CSV format), supporting downstream classification, segmentation, and ensemble learning tasks.

The input image is denoted as $I \in R^{(h\times w\times c)}$, where h represents height, w denotes width, and c indicates channels. Each base CNN model is denoted by $f_m(\cdot)$ where $m \in \{R, V, D\}$ corresponds to ResNet50, VGG16 and DenseNet121 maps the input image to a feature vector $x_m = f_m(I) \in R^{d_m}$ with dimensions: $d_R=2048$, $d_V=4096$, $d_D=1024$. Equation (9) expresses the format of each row in the CSV file.

$$R_i = [f_i, x_i^{(1)}, x_i^{(2)}, \text{-----}, x_i^{(d)}, y_i] \quad (9)$$

In this context, d represents the spatial dimensionality of the final feature vectors, while y_i denotes the corresponding class label.

3.3.2 Feature Selection using QPSODE

The QPSODE technique combines the security and convergence control of Differential Equation modelling with the worldwide search capability of QPSO. The optimization procedure seeks to identify the smallest feature set that optimizes classification performance, with particles serving as candidate feature subsets. QPSO is a variant of classical PSO where particles evolve according to quantum mechanics principles [29]. The following steps are involved in a QPSODE approach for feature selection.

Step 1: Initialization:

The QPSODE feature selection method starts by defining an optimization goal: selecting the feature subset that maximizes classification performance. Key parameters include the quantum control parameter (β), number of features, maximum iteration cycles, and differential equation parameters such as learning rate (Δt) and convergence constant (λ

Step 2: Evaluate Fitness Function

After initializing the particle positions and converting them into binary vectors (where each dimension represents whether a feature is selected), each particle's binary vector is used to subset the dataset accordingly. The fitness of a particle is then computed by training a classifier using only the selected features and evaluating its performance through cross-validation. The fitness function is typically designed to maximize classification accuracy or minimize classification error, although it can also incorporate other metrics and feature count. The equation (10) is used to evaluate the fitness function.

$$Fitness = w_1 \times \text{classification error} + w_2 \text{ X } \left(\frac{Number\ of\ selected\ features}{Total\ features}\right) \quad (10)$$

Where w_1 and w_2 are weights to balance accuracy vs feature subset size.

Step 3: Particle Position Update

The position update equation in QPSO typically involves a probabilistic element based on the local attractor (C_i) and a characteristic length ($L_i(tm)$) that shrinks over time, guiding convergence. Equation (11) updates the location of each element at time tm+1.

x_i (tm+1) =C_i(tm)±β. L_i(tm). In $\left(\frac{1}{u}\right)$ (11)

where x_i (tm+1) is the position of particle i at the next iteration, C_i(tm) is the local attractor for particle i at time tm, often a random point between the particle's personal best ($pBest_i$) and the global best (gBest), β is a contraction expansion coefficient, L_i(tm) is a parameter related to the search range, often proportional to the distance between $pBest_i$ and gBest. The local attractor Ci (tm) is often calculated by the following equation (12).

C_i(tm)=ϕ· $pBest_i$ (tm)+(1−ϕ) · gBest (tm) (12)

where ϕ is a consistently distributed random number between 0 and 1. To compute the mean best position (mBest) and L_i(t), the following equation (13) and (14) are used.

$$\text{mbest(tm)}=\frac{1}{n}\sum_{i=1}^{N} pBest_i\text{(tm)} \quad (13)$$

$$L_i\text{(tm)}= \left| x_i\text{(tm)} - \text{mbest(tm)} \right| \quad (14)$$

Step 4: Differential Equation Modelling:

After the quantum update, we refine the position using a differential equation to introduce dynamic, smooth convergence. After QPSO movement, we define the differential updates to each particle by the equation (15).

$$\frac{dx_i}{dtm}=-\nabla f(x_i)+\lambda(\text{gBest}-x_i) \quad (15)$$

where ∇f(x_i) approximates the fitness landscape gradient, gBest is the global best particle position and λ controls convergence speed. This adds a fine-tuned, deterministic flow toward the optimum, helping guide particles more precisely. The discrete-time implementation is determined by the equation (16).

$$x_i\text{(tm+1)} = x_i\text{(t)}+\Delta t\cdot(-\nabla f(x_i\text{(tm)}) + \lambda(\text{gBest}-x_i\text{(tm)})) \quad (16)$$

Step 5: Update pBest and gBest:

- Update the pBest if its new location results in improved fitness.
- Update gBest if any particle achieves a better global fitness.

Step 6: Stopping Criteria:

- Stop if maximum iterations are reached or if the improvement in gBest fitness is below a small threshold for several iterations.

Step 7: Output:

- The best feature subset corresponding to gBest is returned.

3.3.3 Building Enhanced Blending Classification using RKNODE M-Net

Step 1: Suppose we have used three base models f_1, f_2 and f_3 trained on brain CT images. We obtain base model outputs by the following equation (17).

$$z=(f_2(x), f_2(x), f_3(x)) \in R^k \quad (17)$$

z becomes the input to the meta-model.

Step 2: Build a Meta Model using RKNODE M-Net

The meta-model is not a traditional classifier. It is a neural network whose hidden layers evolve according to the RK method. Simple layer-wise transformations is $h_{i+1}=\sigma(W_ih_i+b_i)$, the hidden state h(tm) as evolving over a continuous time using an ODE. RK approximates the solution at each step tm→tm+h two evaluations. The hidden state evolves according to equation (18).

$$\frac{dh(tm)}{dt}=f(h(tm), tm; \theta) \quad 18)$$

where f is a learnable neural network parameter by weights θ using Fourth-Order Runge-Kutta. To calculate the value of k1, k2 and update the size, the following equations (19), (20) and (21) are used.

$$k_1=f(h(tm), tm) \quad (19)$$

$$k_2=f(h(tm)+\frac{h}{2}k_1, t+\frac{h}{2}) \quad (20)$$

Then update the size,

$$h(tm+h) =h(tm)+h\cdot k_2 \quad (21)$$

If f is a neural network, h is its step size, and h(t) represents the hidden state. To predict the haemorrhage class, A final CNN layer is traversed by the last hidden vector and the result is determined using equation (22).

$$y= \text{Softmax } (W.\ h_{final}+b) \quad (22)$$

The RK Neural ODE meta-model is trained end-to-end via backpropagation through its ODE solver, often using an adjoint sensitivity method for memory efficiency. This allows the meta-model to aggregate diverse CNN features and learn a smoother, continuous feature transformation that optimally separates classes in the latent space [30]. The RK Neural ODE meta-model dynamically captures subtle and noisy feature variations, improving ensemble generalization on complex brain hemorrhage images compared to static classifiers.

3.4 Cloud Environment

Cloud storage plays a vital role in managing large-scale medical image data, intermediate outputs, trained models, and deployed inference services, with object storage being particularly suitable for CT image datasets [31][32]. Deploying the model on the cloud enables scalable processing of large medical image datasets, faster inference using high-performance computing resources, remote accessibility for clinicians, and seamless model updates, making the system practical for real-world clinical use.

4. Experimental Setup

The performance of our proposed cloud-based framework was evaluated using the RSNA dataset of CT images. For comparison with a non-cloud environment configuration, the suggested detection model was set up on an Amazon EC2 instance in the Asia-Pacific region (Tokyo) utilizing Platform as a Service. The primary motivation for utilizing the cloud environment was to reduce both training and testing execution times, enhance model accuracy, and enable remote access from anywhere at any time.

The virtual machines used in the cloud setup ran on the Ubuntu operating system and were powered by Intel(R) Xeon(R) CPU E5-2686 v4 @ 2.30GHz processors. In the non-cloud environment, the experiments were conducted using Python, leveraging libraries such as Torchvision, Keras and TensorFlow within the PyCharm IDE. The system was equipped with GPU acceleration, 201 GB of RAM, and operated on the Windows platform. Accuracy, Precision, Recall, F1-score, and ROC-AUC are the five main metrics used to evaluate the performance of the detection method. The true positive, false positive and true negative, false negative are the four categorization outcomes from which these metrics are constructed. A comparison of the outcomes from the non-cloud and cloud environments is given in this section.

4.1 Qualitative Results and Analysis for Segmentation

The figure 2 compares the performance of the classical U-Net and the proposed RKNODE U-Net showing consistent improvements across Dice, IoU, Precision, and Recall metrics. The RKNODE U-Net achieves higher scores in all metrics demonstrating its superior capability in accurately segmenting hemorrhagic regions.

4.2 Quantitative Results and Analysis for Classification

The figure 3 illustrates a clear performance improvement from Original CT to Masked CT and ROI Proposed inputs, with consistent gains in accuracy, sensitivity, specificity, and AUC. The ROI-based approach achieves the highest scores across all metrics, confirming the effectiveness of segmentation-guided inputs for hemorrhage classification. (b) shows that the decreasing losses demonstrate that the model learns meaningful features and achieves stable performance as training advances.

4.2 Performance Analysis on Non-Cloud and Cloud Environments

The table 2 compares the performance of the proposed classification method in non-cloud and cloud environments. The cloud-based implementation achieves superior results across all evaluation metrics, with accuracy improving from 92.98% to 97.66%, ROC-AUC increasing from 94.2% to 96.28%, and notable gains in precision, recall, and F1-score. In addition to improved predictive performance, the cloud environment significantly reduces computational time, cutting prediction time per epoch from 23 seconds to 9 seconds. These results demonstrate that cloud deployment not only enhances classification accuracy and robustness but also offers faster and more efficient model execution compared to a non-cloud setup.

The figure 4 shows that the comparison of testing accuracy for different intracranial hemorrhage types in non-cloud and cloud environments. The cloud setup consistently achieves higher performance across all categories. For subdural, epidural, intraventricular, intraparenchymal, and subarachnoid hemorrhages, the cloud-based model outperforms the non-cloud environment, with particularly high accuracies observed for intraventricular and subarachnoid cases. Overall, the average accuracy improves from about 92.98% in the non-cloud environment to 97.66% in the cloud environment, demonstrating that cloud deployment provides superior computational efficiency, scalability, and more stable inference, leading to more reliable and accurate hemorrhage classification across all types.

5.3 Comparative Analysis

Table 3 compares brain hemorrhage detection methods in non-cloud and cloud environments in terms of dataset size, accuracy, and execution time. In non-cloud settings, existing classification-based methods achieved accuracies between 89.5% and 99.5%. The proposed segmentation–classification approach attained 92.98% accuracy with an execution time of 23 seconds per epoch on 24,649 images. In cloud environments, prior methods reported accuracies from 92.48% to 98.68%, while the proposed method achieved superior performance with 97.66% accuracy and reduced execution time of 9 seconds per epoch, demonstrating the effectiveness of cloud deployment with segmentation support.

5.4 Statistical Analysis

The proposed RKNODE M-Net framework's performance gains were verified through a statistical investigation. The classification accuracy results across the five hemorrhage types were compared between the standard model and RKNODE M-Net using a paired t-test to assess significance and consistency of improvements. From the formula we get the t-test statistic value of 9.84, and from the table we get the t-rate of 2.132. Since t is greater than 2.132, we reject H_0 at the 5% level of significance. Therefore, we conclude that blending-based RKNODE M-Net architecture is superior to standard meta networks. Figure 6 shows the graphical representation of the significant differences in accuracy between different groups of images.

Table 1: *Overview of Previous Studies on Disease Detection*

Authors	Methodology	Method	Limitation	Metrics (%)
[20]	Sub-Net 1, 2 and 3	Classification	Performance metrics was not calculated clearly	Acc=99.5
[21]	VGG version 16 & 19, RES50, INV3, XCEP, MOBN and INRESV2.	Classification	High Computational complexity due to the training and testing.	Acc=93.8
[22]	MPF-DNN + ResNet101 + SVM	Classification	Feature Selections are not mentioned	Acc=95.82
[23]	EnsCVDD-Net and BlCVDD-Net	Classification	Large dataset and not focused on segmentation	Acc=88 & 91
[24]	ResNet50 and DenseNet201	Classification	Small and unbalanced Data Set	Acc=92
[25]	nmODE-KD	Segmentation	Not focused on preprocessing and Imbalanced Data Set	DSC=0.8304
[26]	Improved U-Net:	Segmentation	Prediction value is low	DSC=82 & JCOE= 80
[27]	U-Net with a masked loss function	Segmentation	Data set size is small	DSC=76 Sen=77 and Spec= 96
[28]	IHA Net	Segmentation	error value deterioration	Jaccard Index=0.6 and DSC=0.7.

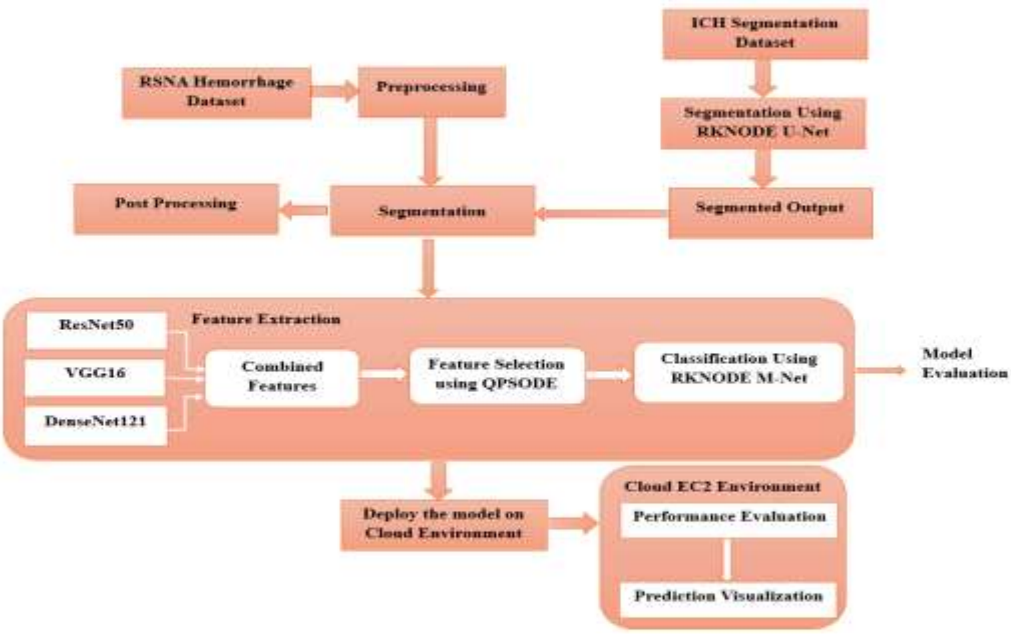

Figure 1: *Proposed Frame Work Architecture for hemorrhage Detection*

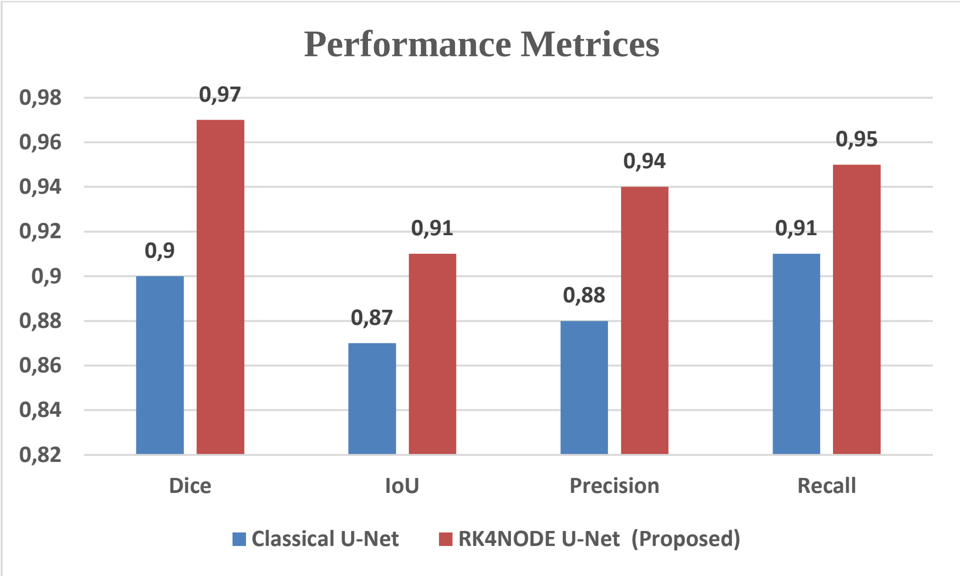

Figure 2: *Segmentation Performance on PhysioNet Dataset*

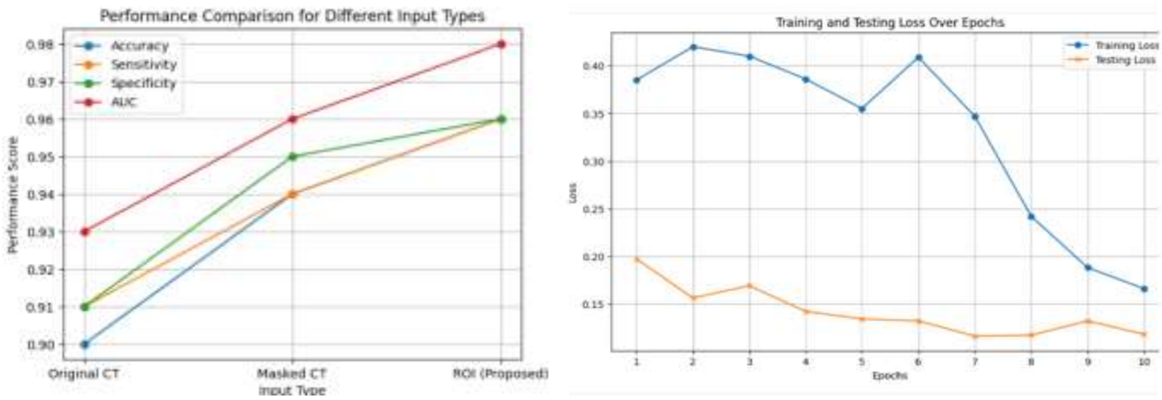

(a) **(b)**

Figure 3 *(a) & (b): RSNA Classification Performance*

Table 2: *Simulation Results of Classification on Non-Cloud and Cloud Environment*

Proposed Method	Accuracy (%)	Precision (%)	Recall (%)	F1-Score (%)	ROC-AUC (%)	Prediction Time (sec)/Epoch
Classification on Non-Cloud Environment	92.98	93.11	92.5	93.06	94.2	23
Classification on Cloud Environment	97.66	96.44	93.91	94.15	96.28	9

Table 3: *Non-Cloud vs. Cloud: Comparative Analysis of the Proposed and Existing Methods*

Environment	Authors	No of Images	Method	Testing Accuracy	Prediction Time (sec) /Epoch
Non-Cloud	[17]	4500	Classification	99.5	-
	[18]	7,909		93.8	-
	[19]	2800		95.82	-
	[21]	696		92	-
Cloud	[26]	569		98.68	-
	[27]	2400		92.48	-
	[28]	623	Classification & Segmentation	97.1	-
Non-Cloud	**Proposed**	**24,649**	**Segmentation & Classification**	**92.98**	**23**
Cloud	**Proposed**	**24,649**	**Segmentation & Classification**	**97.66**	**9**

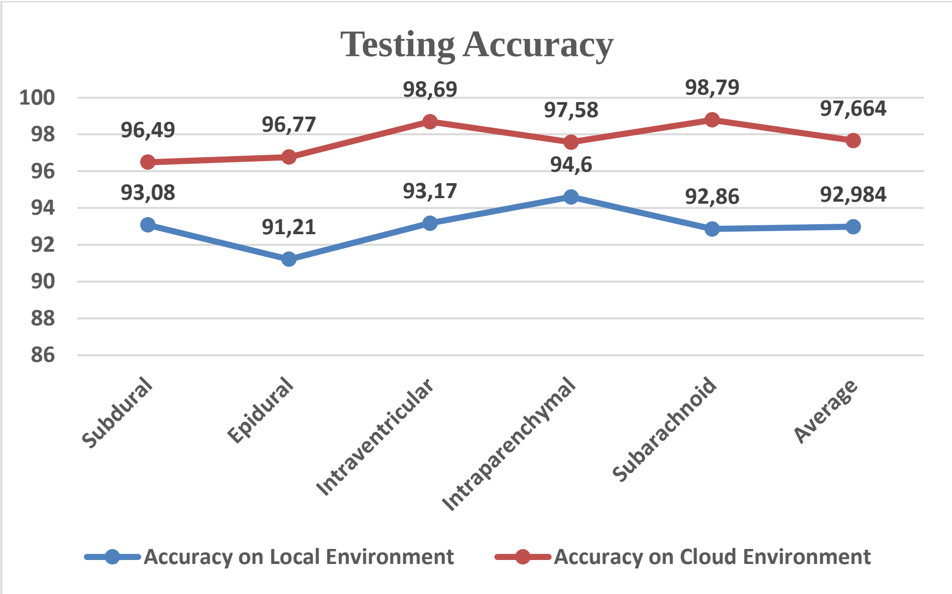

Figure 4: *Accuracy with different hemorrhage types on Non-Cloud and Cloud Environment*

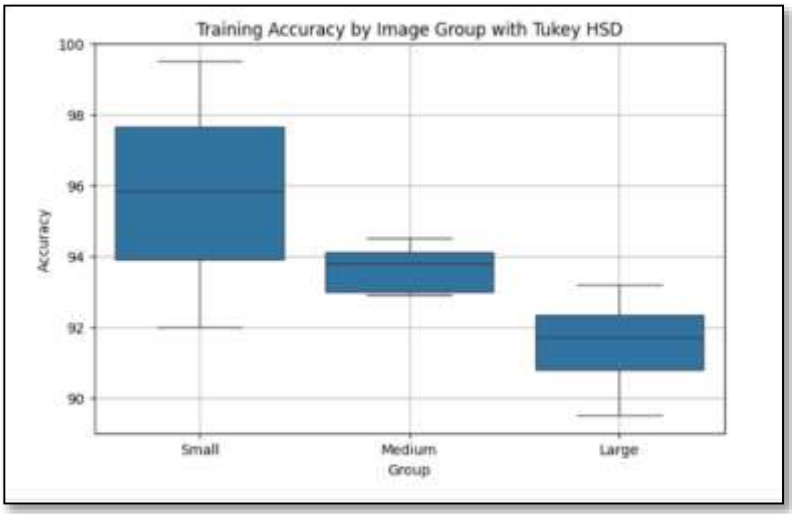

Figure 6: *Report for Analysis of Variance*

6. Conclusions

This study presents an efficient and scalable framework for RSNA hemorrhage detection, combining an RKNODE U-Net for precise segmentation with an enhanced blending RKNODE M-Net for robust multi-class classification. This system significantly boosts segmentation and classification performance in both non-cloud and cloud environments. By integrating advanced preprocessing, RK-based Neural ODE architectures, and ensemble learning, the framework achieves faster execution, improved generalization, and higher accuracy. The framework is enhanced by QPSODE, which facilitates effective and robust feature selection in high-dimensional data. The RKNODE U-Net's deeper and more stable feature learning in the bottleneck phase, coupled with self-calibrated convolutional mechanisms, enhances the capture of complex spatial variations and improves contextual awareness and boundary delineation in hemorrhagic regions. Cloud deployment further ensures scalability and real-time accessibility, making it suitable for large-scale medical imaging. Experimental results show that the RKNODE M-Net outperforms standard approaches in individual and average classification. The system's computing efficiency and 9 seconds execution time make it ideal for real-time or large-scale clinical deployment and a dependable brain hemorrhage computer-aided diagnostic tool.

Future work aims to enhance the model's diagnostic accuracy by integrating multi-modal MRI and CT imaging inputs, leveraging their complementary strengths. To optimize training efficiency, preprocessing and augmentation steps could be migrated to a cloud environment. Further accuracy improvements can be achieved by fine-tuning classification parameters and ensuring generalizability through validation across diverse real-world clinical datasets. The framework will be deployed and evaluated across various cloud virtual machine configurations to analyze performance, cost, and scalability trade-offs.

Author Statements:

- **Ethical approval:** The conducted research is not related to either human or animal use.
- **Conflict of interest:** The authors declare that they have no known competing financial interests or personal relationships that could have appeared to influence the work reported in this paper
- **Acknowledgement:** The authors declare that they have nobody or no-company to acknowledge.
- **Author contributions:** The authors declare that they have equal right on this paper.
- **Funding information:** The authors declare that there is no funding to be acknowledged.
- **Data availability statement:** The data that support the findings of this study are available on request from the corresponding author. The data are not publicly available due to privacy or ethical restrictions.
- **Use of AI Tools:** The author(s) declare that no generative AI or AI-assisted technologies were used in the writing process of this manuscript.

References

[1] X. Wang et al., "A deep learning algorithm for automatic detection and classification of acute intracranial hemorrhages in head CT scans," *NeuroImage Clin*., vol. 32, p. 102785, 2021.

[2] M. Rajagopal et al., "An efficient framework to detect intracranial hemorrhage using hybrid deep neural networks," *Brain Sci*., vol. 13, no. 3, p.400, 2023.

[3] S. N. Ahmed and P. Prakasam, "A systematic review on intracranial aneurysm and hemorrhage detection using machine learning and deep learning techniques," Prog. *Biophys. Mol.* Biol., vol. 183, pp. 1–16, 2023.

[4] G. Kasinathan and S. Jayakumar, "Cloud-based lung tumor detection and stage classification using deep learning techniques," *Biomed*. Res. Int., vol.2022, no. 1, p. 4185835, 2022.

[5] B. C. Anil et al., "Efficient local cloud-based solution for liver cancer detection using deep learning," Int. J. *Cloud Appl. Comput*. (IJCAC), vol.12, no. 1, pp. 1–13, 2022.[6] V. Lahoura et al., "Cloud computing-based framework for breast cancer diagnosis using extreme learning machine," *Diagnostics*, vol. 11, no. 2, p.241, 2021.

[7] M. Guzel, A. Yildiz, S. Dogan, and F. Cagatay, "Cloud type classification using deep learning with cloud images," *PeerJ Comput. Sci*., vol. 10, p.e1779, 2024.

[8] M. A. Ganaie et al., "Ensemble deep learning: A review," *Eng. Appl*. Artif.Intell., vol. 115, p. 105151, 2022.

[9] L. Kong and J. Cheng, "Classification and detection of COVID-19 X-Ray images based on DenseNet and VGG16 feature fusion," *Biomed*. Signal Process. Control, vol. 77, p. 103772, 2022.

[10] M. Zhu, B. Chang, and C. Fu, "Convolutional neural networks combined with Runge–Kutta methods," *Neural Comput*. Appl., pp. 1629–1643, 2023.

[11] T. V. S. S. Chaitanya et al., "Numerical solution of first and second order differential equations with deep neural networks," in Proc. *IEEE World Conf. Appl*. Intell. Comput. (AIC), 2023.

[12] C.-W. Cheng et al., "Continuous U-Net: faster, greater and noiseless,"arXiv preprint arXiv:2302.00626, 2023.

[13] A. Hussain et al., "An attention-based ResNet architecture for acute hemorrhage detection and classification: Toward a Health 4.0 digital twin study," *IEEE Access*, vol. 10, pp. 126712–126727, 2022.

[14] T. D. Phong et al., "Brain hemorrhage diagnosis by using deep learning,"in Proc. 2017 Int. Conf. Mach. Learn. *Soft Comput*., 2017.

[15] S. Nizarudeen and G. R. Shanmughavel, "Comparative analysis of ResNet,ResNet-SE, and attention-based RaNet for hemorrhage classification in CT images using deep learning," *Biomed.* Signal Process. Control, vol. 88, p.105672, 2024.

[16] B. Vamsi et al., "Early detection of hemorrhagic stroke using a lightweight deep learning neural network model," *Trait. Signal*, vol. 38, no. 6, 2021.

[17] M. I. H. Emon et al., "Intracranial brain hemorrhage diagnosis and classification: A hybrid approach," *in Proc. 6th Int. Conf. Inf. Comput. Technol. (ICICT), IEEE*, 2023.

[18] A. Abdullah, W. S. Wong, and D. Albashish, "EB-CNN: Ensemble of branch convolutional neural network for image classification," *Pattern Recognit. Lett*., vol. 189, pp. 1–7, 2025.

[19] A. H. Barshooi, "IoT-based classification and differential diagnosis of COVID-19 from CT images using DexiNed filter, image blending and weighted ensemble CNNs," *in Proc. 9th Int. Conf. Web Res. (ICWR), IEEE*, 2023.

[20] I. U. Haq et al., "Feature fusion and ensemble learning-based CNN model for mammographic image classification," *J. King Saud Univ.-Comput. Inf.Sci*., vol. 34, no. 6, pp. 3310–3318, 2022.

[21] H. Zerouaoui, A. Idri, and O. E. Alaoui, "Assessing the impact of deep end-to-end architectures in ensemble learning for histopathological breast cancer classification," in *KDIR*, 2022.

[22] H. Uzen, M. Turkoglu, and D. Hanbay, "Texture defect classification with multiple pooling and filter

ensemble based on deep neural network," *Expert Syst. Appl*., vol. 175, p. 114838, 2021.

[23] H. Khan et al., "heart disease prediction using novel ensemble and blending based cardiovascular disease detection networks: EnsCVDD-Net and BlCVDD-Net," *IEEE Access*, 2024.

[24] B. S. Deo et al., "An ensemble deep learning model with empirical wavelet transform feature for oral cancer histopathological image classification,"*Int. J. Data Sci. Anal*., 2024, pp. 1–18.

[25] J. Hu et al., "Enhancing robustness of medical image segmentation model with neural memory ordinary differential equation," Int. J. Neural Syst., vol. 33, no. 12, p. 2350060, 2023.

[26] Y. Yuan et al., "Computed tomography image segmentation of irregular cerebral hemorrhage lesions based on improved U-Net," J. *Radiat. Res.Appl*. Sci., vol. 16, no. 3, p. 100638, 2023.

[27] N. A. Coorens et al., "Intracerebral hemorrhage segmentation on noncontrast computed tomography using a masked loss function U-Net approach,"J. *Comput. Assist. Tomogr*., vol. 47, no. 1, pp. 93–101, 2023.

[28] Y. Ma et al., "IHA-Net: An automatic segmentation framework for computer-tomography of tiny intracerebral hemorrhage based on improved attention U-Net," *Biomed*. Signal Process. Control, vol. 80, p. 104320, 2023.

[29] E. I. Elsedimy, S. M. M. AboHashish, and F. Algarni, "New cardiovascular disease prediction approach using support vector machine and quantumbehaved particle swarm optimization," *Multimedia Tools Appl*., vol. 83, no.8, pp. 23901–23928, 2024.

[30] E. Giesecke and A. Kr¨oner, "Classification with Runge-Kutta networks and feature space augmentation," arXiv preprint arXiv:2104.02369, 2021. [Online]. Available: https://arxiv.org/abs/2104.02369

[31] G. Kasinathan and S. Jayakumar, "Cloud-based lung tumor detection and stage classification using deep learning techniques," *Biomed. Res*. Int., vol.2022, no. 1, p. 4185835, 2022.

[32] Lanjewar, Madhusudan G., Arman Yusuf Shaikh, and Jivan Parab. "Cloud-based COVID-19 disease prediction system from X-Ray images using convolutional neural network on smartphone." *Multimedia Tools and Applications* 82.19 (2023): 29883-29912.